Cryogenics 74 (2016) 131–137

Contents lists available at ScienceDirect

Cryogenics

journal homepage: www.elsevier.com/locate/cryogenics

A new experiment for investigating evaporation and condensation of cryogenic propellants

K. Bellur [a], E.F. Médici [a], M. Kulshreshtha [a], V. Konduru [a], D. Tyrewala [a], A. Tamilarasan [b], J. McQuillen [c], J.B. Leão [d], D.S. Hussey [d], D.L. Jacobson [d], J. Scherschligt [d], J.C. Hermanson [b], C.K. Choi [a], J.S. Allen [a,*]

[a] Michigan Technological University, 1400 Townsend Drive, Houghton, MI, USA
[b] University of Washington, Seattle, WA, USA
[c] NASA Glenn Research Center, 21000 Brookpark Road, Cleveland, OH, USA
[d] National Institutes of Standards and Technology, Gaithersburg, MD, USA

ARTICLE INFO

Article history:
Received 24 June 2015
Received in revised form 17 October 2015
Accepted 19 October 2015
Available online 30 October 2015

Keywords:
Evaporation
Condensation
Liquid hydrogen
Neutron imaging
Contact angle

ABSTRACT

Passive and active technologies have been used to control propellant boil-off, but the current state of understanding of cryogenic evaporation and condensation in microgravity is insufficient for designing large cryogenic depots critical to the long-term space exploration missions. One of the key factors limiting the ability to design such systems is the uncertainty in the accommodation coefficients (evaporation and condensation), which are inputs for kinetic modeling of phase change.

A novel, combined experimental and computational approach is being used to determine the accommodation coefficients for liquid hydrogen and liquid methane. The experimental effort utilizes the Neutron Imaging Facility located at the National Institute of Standards and Technology (NIST) in Gaithersburg, Maryland to image evaporation and condensation of hydrogenated propellants inside of metallic containers. The computational effort includes numerical solution of a model for phase change in the contact line and thin film regions as well as an CFD effort for determining the appropriate thermal boundary conditions for the numerical solution of the evaporating and condensing liquid. Using all three methods, there is the possibility of extracting the accommodation coefficients from the experimental observations. The experiments are the first known observation of a liquid hydrogen menisci condensing and evaporating inside aluminum and stainless steel cylinders. The experimental technique, complimentary computational thermal model and meniscus shape determination are reported. The computational thermal model has been shown to accurately track the transient thermal response of the test cells. The meniscus shape determination suggests the presence of a finite contact angle, albeit very small, between liquid hydrogen and aluminum oxide.

1. Introduction and background

Passive and active thermal and fluid control systems are routinely used to manipulate cryogenic liquids in microgravity and to mitigate boil off. Computational fluid dynamics (CFD) modeling of the propellant coupled with a lumped thermodynamic treatment of the vapor phase has been used to study pressurization within cryogen tanks [1–5]. From these models, a thin (approximately 1 mm) liquid layer separating the vapor phase from the wall was shown to form. Accurately predicting the stability of the liquid layer and evaporation/condensation remains a challenge due to the absence of reliable values of evaporation and condensation coefficients and the ability to computationally capture the local thermodynamics [1,5,6].

Additional experimental evidence that suggests understanding local thermodynamic states is critical to predicting phase change of liquid hydrogen and methane were found during recent tests conducted at National Aeronautics and Space Administration (NASA) Glenn Research Center located in Cleveland, Ohio. These experiments focused on determination of bubble-point pressure, i.e. vapor break through, for liquid oxygen, methane, and hydrogen in liquid acquisition screens. The uncertainty in the experimental data was largely attributed to uncertainty in the evaporation at the screen surface [6–8]. Meniscus phase change is significantly different than that of pool boiling, where vapor pressure and wall temperature are generally sufficient to predict heat flux. Two additional factors affect phase change at a meniscus, such as those

* Corresponding author.
E-mail address: jstallen@mtu.edu (J.S. Allen).

http://dx.doi.org/10.1016/j.cryogenics.2015.10.016
0011-2275/

present in a screen. The first is curvature, which gives rise to a pressure jump across the liquid–vapor interface due to surface tension. The second factor is the presence of the contact line, which results in non-uniform evaporation over the liquid surface due to anisotropy in the liquid stresses within the thin liquid film due to disjoining pressure effects [9]. Curvature and disjoining pressure effects have been incorporated into evaporation and condensation models [9–12], but accurate measures of the evaporation and condensation coefficients remains a challenge, especially for cryogenic liquids.

Liquid–vapor (evaporation or condensation) phase change is a complex, multiscale, conjugate problem. Different phase change models have been proposed to quantify the rate of mass transfer form one state to the other. These models can be classified as diffusive or kinetic models. Diffusive models rely upon relative partial pressure for triggering phase change. Diffusive evaporation or condensation models are material independent, generating the same mass flux regardless of the contact angle or liquid phase curvature. These models have been applied to study phase change in liquid reservoirs with large open surface area. In contrast, models traditionally used for investigating phase change in smaller liquid reservoirs where the exposed surface is comparable to the meniscus size, such as in porous media, are kinetics based. Kinetic models are dependent upon the material properties, the location of liquid phase within the material and may take into account the effect of disjoining pressure, meniscus curvature, and non-equilibrium interface temperature [13].

When evaporation is diffusion limited, the rate of phase change is proportional to the interfacial area and to the concentration difference between the vapor and the liquid–vapor interface, which for the modeling purposes is considered to be saturated vapor. A change in substrate material has no effect on the rate of phase change. As the interfacial area decreases with respect to contact line length, the rate of evaporation is no longer proportional to the area and a different model is needed to predict the mass flux based on the molecular dynamics taking place at the contact line region.

The contact line is an apparent intersection of three phases – vapor, liquid and solid. This intersection is commonly described using the static contact angle, θ, which refers to the apparent angle between the liquid and the solid (as measured through the liquid). The contact line is a continuum region and is often described for wetting liquids as a continuously thinning film that terminates in an absorbed layer. Fig. 1 delineates regions of interest along a wetting evaporating meniscus according to the component of normal stress most affecting the thermo-fluid dynamics. The normal stress in the bulk liquid is mostly affected by capillarity, or interface curvature. The adsorbed film region is characterized by intermolecular forces and is not optically accessible. Both intermolecular forces and curvature affect the normal stress in the contact line region. A typical value of the maximum thickness of the contact line region where intermolecular forces begin to affect the liquid interface shape is 1 μm.

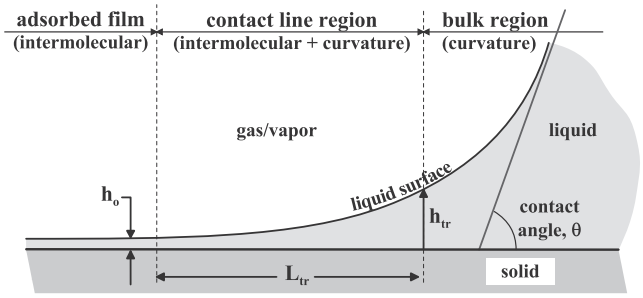

Fig. 1. Extended meniscus with regions delineated by normal stress components.

The contact line region has a dramatic effect on evaporation (and condensation). Typically during phase change a relatively large temperature gradient is setup in the contact line region both parallel and perpendicular to the solid surface that may result in thermocapillary stresses. For non-polar and/or wetting liquids, the result is that 60–90% of the total evaporation occurs in the contact line region [9,14–28]. Though specific experiments have been empirically analyzed and numerical models validated against these experiments [9,16,22], the effect of contact angle and contact line length on total evaporation is not quantitatively predictable in a general sense.

A kinetic model depends upon the local interface conditions in the contact line region, specifically in the contact line region. The amount of mass undergoing phase change is proportional to the size of the contact line region as well as the local properties such as partial pressure of vapor, temperature, and relative humidity. The mass undergoing phase change can be expressed in the form of the Hertz–Knudsen–Schrage equation [9,11,29]. Originally developed from kinetic theory for planar evaporation, this model has been expanded to include the effects of surface tension [10] and surface curvature [12] through the use of the Clapeyron equation:

$$J = \frac{2\alpha}{2-\alpha}\left(\frac{M}{2\pi R T_{lv}}\right)^{1/2}\left[\frac{p_v M h_{fg}}{R T_v T_{lv}}(T_{lv}-T_v) - \frac{v_l p_v}{R T_{lv}}(\Pi+\sigma\kappa) + \frac{M g p_v}{R T_v}x\right], \tag{1}$$

where J is the evaporative flux, α is the evaporation or condensation coefficient (often referred to as the accommodation coefficient), T_{lv} is interfacial temperature, Π is the disjoining pressure (the net pressure reduction within the film due to the solid–liquid intermolecular forces), σ is surface tension, and κ is the surface curvature. Other parameters are standard thermodynamic properties [12].

Evaporation and condensation coefficients, often referred to as accommodation coefficients, are derived from kinetic theory and represent the fraction of molecules striking the liquid surface [11]. The accommodation coefficient is considered to be a thermodynamic property of kinetic models of evaporation and condensation. Accurate prediction of the rate of phase change typically requires a measured value of the accommodation coefficient.

Unfortunately, there is significant discrepancy in reported values of the accommodation coefficient. For water alone the values have varied by two to three orders of magnitude depending on the researcher or the method used to determine this coefficient. An indication of why there is such a large discrepancy in the mass accommodation coefficient can be inferred from experiment details described by Cammenga et al. [30] and reiterated in Marek and Straub [31]. An evaporation coefficient of 0.002 was found for water in a glass vessel, but when the glass vessel was replaced with a copper vessel the evaporation coefficients increased two orders of magnitude to values between 0.25 and 0.38. With the exception of the vessel wall material, both experiments were conducted in the same apparatus. Thus, the reported values of the accommodation coefficient do not reflect the local conditions nor the non-uniform evaporation that occurs due to the presence of a contact line.

To solve for the mass flux undergoing phase change the temperature in the liquid phase is required. The liquid temperature depends on the adjacent solid surface temperature. Liquid and solid temperature profiles can be obtained from a conjugate heat transfer model that incorporates representative boundary conditions of the system under observation. For this research, a computational thermal model of the test cell and sample well developed in ANSYS/Fluent is used to obtain the temperature profile on the interior solid surface of the test cell. The liquid temperature profile is obtained through integration of a lubrication

model [27] using the computational results for the thermal boundary conditions. The total mass evaporated, and subsequent heat transfer, is found by integrating Eq. (1) from the adsorbed film region to the bulk meniscus region.

To that end, a new type of experiment with complimentary computational analysis has been undertaken to determining the evaporation and condensation coefficients for liquid hydrogen and methane. A combined modeling and experimental effort is being pursued with the experiments conducted at the Neutron Imaging Facility (NIF) located at the National Institute of Standards and Technology (NIST) located in Gaithersburg, Maryland. Results from evaporation and condensation experiments will be discussed in forthcoming manuscripts. The focus of this manuscript will be restricted to the use of the dry cell tests for calibration of a CFD thermal model and edge detection of liquid hydrogen surfaces inside the aluminum and stainless steel test cells.

2. Neutron imaging experiments

Experiments examining the bulk evaporation and condensation of liquid hydrogen were conducted during January 2015 at the NIST Center for Neutron Research (NCNR) in the Neutron Imaging Facility. Thermal neutrons ($E \approx 25$ meV) neutrons from a fission reactor penetrate a cryostat that contains a steel or aluminum test apparatus. The large neutron scattering cross section of hydrogen as compared to that of steel and aluminum allows for signal-to-noise levels sufficient for imaging the location of the liquid hydrogen surface within the test cells.

The scintillator used for imaging is a 7.6 mg/cm^2 Gadoxysulfide screen with a thickness of 20 μm. An Andor NEO sCMOS (scientific Complementary Metal Oxide Semiconductor) camera with a pixel pitch of 6.5 μm and variable exposure time is used to capture the images. An 85 mm Nikon lens with a PK13 extension tube was used to image the scintillator light. This detector configuration has sufficient spatial (< 50 μm) and temporal (<10 s) resolution to measure local curvature and evaporation rates of liquid hydrogen. Additional details on the Neutron Imaging Facility (NIF) and the hydrogen infrastructure used for the experiments described herein can be found in Hussey et al. [32,33].

A schematic of the cryostat is shown in Fig. 2. The sample well passes through concentric vacuum and cryogen annuli and then extends below these annuli into an evacuated chamber through which the neutron beam passes. The outer most cryogen annulus is filled with liquid nitrogen that evaporates and vents to the atmosphere thereby maintaining a temperature of 77 K. An inner liquid helium jacket also evaporates. The rate of helium evaporation and therefore the rate of cooling and minimum temperature is controlled through a throttling valve that can be adjusted. For additional cooling a vacuum can be pulled on the vapor side of the throttling valve. The helium throttle valve is part of an assembly referred to as the copper block that is positioned at the separation between the cryostat and the lower chamber through which the neutron beam passes. An electric heater is also located in this copper block. In this manner, the temperature of the copper block can be set and controlled. Thermal energy is transferred to and from the test cell (suspended in the bottom of the sample well) by a combination of (i) conduction from the copper block through an aluminum radiation baffle and down a stainless tube to the test cell, and (ii) convection in low pressure helium gas circulating between the test cell and the sample well housing. The stainless tube with radiation baffles to which the test cell is attached is referred to as the sample stick.

The cryostat is prepared by filling with liquid nitrogen and liquid helium to begin the cool down. The sample well is filled with helium gas at approximately 135 kPa absolute (19.6 psia). The

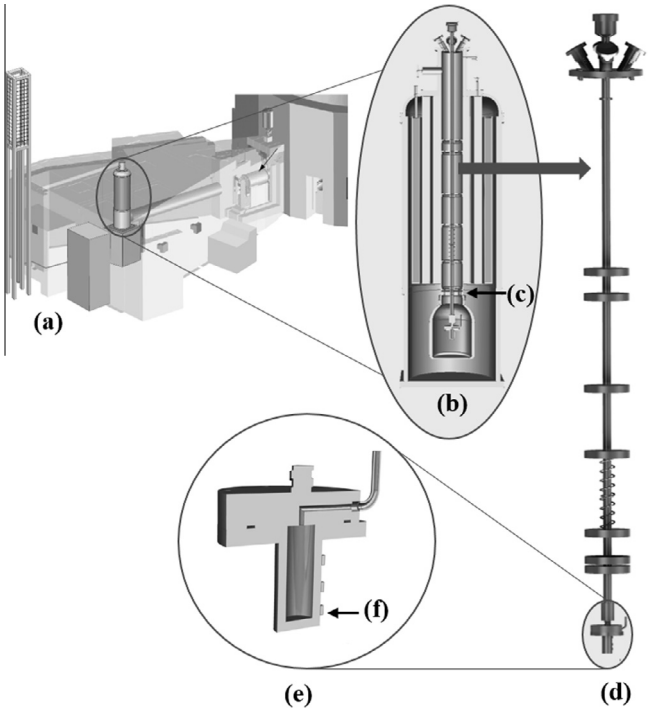

Fig. 2. Overview of experiments conducted at the NIST Neutron Imaging Facility (NIF). (a) Neutron Imaging Facility with cryostat in beam line. (b) Cryostat with test cell installed. (c) Location of copper block used for heating and cooling the test cell and helium gas in the sample well. (d) Sample holder with 10-mm test cell attached. (e) Cutaway view of the 10 mm diameter test cell and lid. (f) Si-diode thermal sensor.

helium is allowed to continuously flow into and out of the sample well so as to prevent the introduction of air or water vapor. While the helium gas is flowing through the sample well, the sample stick with the test cell assembly is inserted and secured with an o-ring seal in the top flange. Then the helium gas is completely evacuated from the sample well to a pressure of 10^{-6} torr and reintroduced at 125–135 kPa absolute. This evacuation and refilling procedure is performed three times in order to thoroughly purge the sample well of any residual air and water vapor that might form an ice blockage and prevent free movement of the sample stick. Following the last evacuation of the sample well, a small quantity of helium gas is reintroduced with a pressure between 10 Pa and 200 Pa absolute. At the time of these experiments, the exact pressure of the sample well during testing was not available. Even with this pressure known, however, the density of helium surrounding the test cell would be difficult to determine due to the temperature gradient that exists along the sample well (≈ 20 K) from the test cell up to the flange seal (≈ 300 K). Since the density of the helium in the sample well is not known, a sequence of complimentary experiments and numerical simulations are performed in order to characterize the conductive and convective heat transfer from the cryostat copper block to the test cell. This procedure is discussed later.

A hydrogen generator with a control manifold is used for these tests. For the hydrogen evaporation–condensation experiments, the manifold is configured to allow for three functions. The first is to be able to pull a hard vacuum on the entire manifold and the test cell, which is connected to the manifold via a 1/8 in. diameter stainless steel line. In this manner, the test cell can be evacuated and a leak check performed prior to introduction of the hydrogen. The second function of the manifold is to purge the manifold and the test cell with gaseous helium for pressurized leak checks. Finally, the third function of the manifold is to

Table 1
Test cells used during hydrogen experiments conducted in January 2015 at the NIST Neutron Imaging Facility.

Test cell	Material	Shape	Inner diameter	Wall thickness (mm)	Bond number
1	6061 Al	Conical	5 mm & 30 mm, 10° transition	3	2.3, 84.5
2	316L SS	Cylindrical	10 mm	3	9.3
3	6061 Al	Cylindrical	30 mm	3	84.5
4	6061 Al	Cylindrical	10 mm	3	9.3

introduce hydrogen to the test cell and to accurately control the vapor pressure. For evaporation tests, the vapor pressure established at the manifold is set slightly below the saturation pressure at the temperature set point of the cryostat. Alternatively, the set point of the cryostat can be set above the saturation temperature of the pressure set point of the manifold. For condensation, these conditions are reversed.

Once the leak checks are satisfactorily completed, hydrogen gas is delivered to the manifold at 1380 kPa (200 psig) from the generator. The pressure of the hydrogen gas is decreased using a regulator to between 100 kPa and 200 kPa absolute (15–30 psia). The hydrogen flows continuously through the manifold to the atmospheric vent. The pressure in the gas manifold is adjusted to the desired saturation pressure ±100 Pa (±1 mbar) by throttling the pressure from the manifold to the vent using a needle valve. With this arrangement, hydrogen could be transferred to or from the test cell during condensation or evaporation, respectively, without changing the pressure set point. When testing at hydrogen saturation pressures close to atmospheric pressure, the manifold is vented through a vacuum pump prior to exiting at the atmospheric vent. In this way, there remains sufficient pressure differential across the throttling valve for accurate pressure control.

Four test cell configurations were used during testing. The configurations were varied in order to investigate the effect of (i) surface properties that affect the disjoining pressure term in Eq. (1), (ii) geometric properties that affect the curvature term, and (iii) contact line length to liquid–vapor surface area. Additional design constraints include volume restrictions for safety considerations and diameter constraints for imaging considerations. The latter required that there be sufficient liquid–vapor interface curvature so that there was never the possibility of interface-pixel alignment; that is, the liquid–vapor interface never aligns with a single row of pixels. This condition would result in a large uncertainty in the interface location since the pixel dimensions are 25 μm. In addition, the diameter of the test cell needed to be large enough that there were sufficient pixels across the interface for accurate edge detection. This latter condition was met by maintaining a Bond number between 1 and 100. The Bond number is defined as $\Delta\rho g r^2/\sigma$, where $\Delta\rho$ is the density difference across the liquid–vapor interface, g is gravitational acceleration, r is the radius of the test cell, and σ is surface tension. Table 1 lists the pertinent details of each test cell.

The first test cell is a 5 mm diameter cylinder connected to a 30 mm diameter cylinder through a conical section with a 10° slope from the horizontal. Fig. 3a illustrates this test cell. The remaining three of the test cells are cylindrical in shape. One purpose of the conical test cell was to investigate the possible existence of a finite contact angle with hydrogen on aluminum, which was suggested from preliminary experiments conducted in September 2014. The preliminary experiments suggested a contact angle as large as 10°. If this condition were to exist, then the liquid–vapor interface should be perfectly flat in the 10° conical transition regardless of the Bond number. From Fig. 3a, the interface is indeed flat in this region. While suggestive of a finite contact angle, a more quantitative analysis of interface curvature and the possibility of a finite contact angle is discussed later. All test cells used a common lid fabricated from 316L stainless steel. The test cell lid includes a vapor passage that is also shown in Fig. 3a.

The four test cells and stainless steel lid were cleaned using an acid solution, which is made from sulfuric acid (H_2SO_4, 96% concentration) and hydrogen peroxide (H_2O_2, 35% concentration) in 3:1 volumetric ratio, respectively. The parts to be cleaned were immersed in the acid solution for 10–20 s after which these were immediately immersed in a beaker with 90 °C distilled water. The part was then immersed in another beaker with distilled water at room temperature. After rinsing with distilled water, the components are blown clear of any residual water using dry nitrogen, allowed to cool and sealed in plastic bags. For the aluminum test cells, this procedure results in an oxide formation and an increase in the surface roughness. The mean surface roughness is between 1 μm and 10 μm.

Instrumentation for these experiments consisted of pressure measurements on the test cell feed line and manifold as well as temperature measurements on the test cell exterior, the helium in the sample well, and the cryostat. Three Lakeshore silicon diode DT-670 temperature sensors were mounted on the outside of the test cell and secured in place by use of custom fabricated 306 stainless steel springs that wrapped around the test cell exterior. A fourth sensor was suspended in the sample well near the test cell to measure the temperature of the circulating helium gas. Test cell temperatures were logged using a Lakeshore Model 340. Calibration curves incorporated into the Lakeshore Model 340 for this series of sensor were used for converting the sensor signals to temperatures. The uncertainty in the test cell temperature measurements is ±0.25 K. The uncertainty in the cryostat heater temperature is ±0.1 K. The temperature of the copper block (NTC

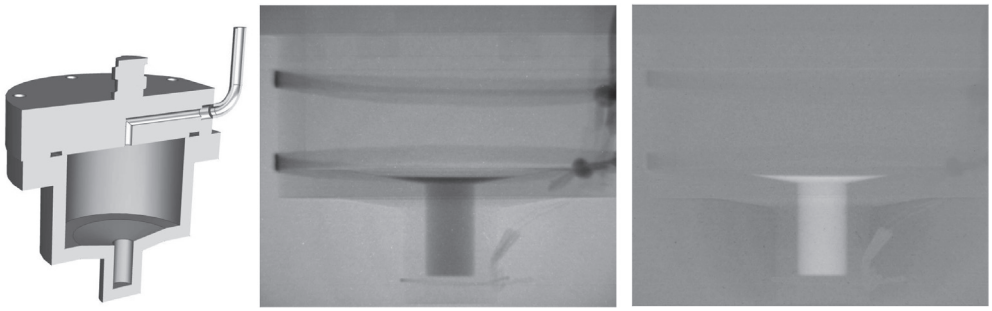

(a) Conical test cell & lid. **(b)** LH_2 in conical section. **(c)** Image normalized.

Fig. 3. (a) Cutaway view of conical test cell. The smaller cylinder is 5 mm diameter and the larger cylinder is 30 mm diameter. The conical section has a 10° slope from the horizontal. (b) Liquid hydrogen in an aluminum 6061 test cell. A silicon diode sensor attached to the 5 mm diameter section is faintly visible. The flat hydrogen interface in the conical portion indicates the presence of a contact angle of approximately 10°. (c) Normalized image emphasizing liquid hydrogen location.

RTD X45720 sensor) and the sample holder temperature (Scientific Instruments Si410B sensor) were logged using a Lakeshore Model 331 that was also used to control the heater temperature. Pressures were logged using two Mensor pressure transducers. One sensor (Mensor CPG 2500) was connected to the hydrogen gas feed connected to the test cell. The second pressure transducer (Mensor DPG 15000) was connected to the manifold. The uncertainty in the pressure measurements is 0.01% of the reading.

For each test cell, three types of experiments were conducted – dry cell, condensation, and evaporation. The 'dry cell' tests were conducted to provide transient thermal response data to be used later in calibrating the computational thermal model. A vacuum of 10^{-6} torr was pulled on the manifold which was open to the test cell. While under continuous vacuum, the temperature of the test cell was increased and decreased by adjusting the cryostat set point.

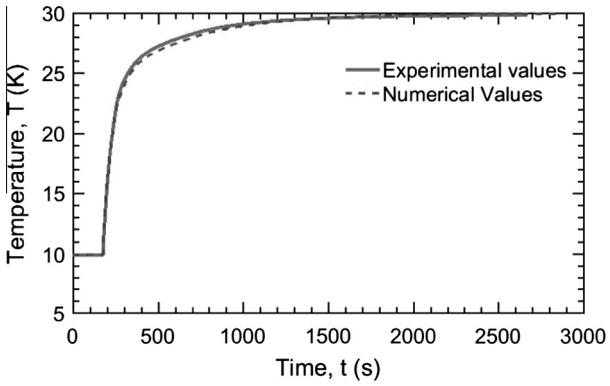

Fig. 4. Experimental and numerical time response for the dry cell experiment with the 10 mm diameter 316L SS test cell.

3. Thermal modeling of test cells

The design of the experiment is such that no temperature measurements can be made on the inside of the test cell and no transient heat transfer data are available for the cryostat. In order to extract the evaporation and condensation coefficients, the evaporation model (Eq. (1)) requires a thermal boundary condition on the interior wall of the test cell. In order to determine the appropriate interior wall temperature distribution, an axisymmetric computational thermal model was developed using ANSYS/Fluent. Coupling of pressure and velocity is achieved using the SIMPLEC (Semi Implicit Method for Pressure Linked Equations Coupled) algorithm and the convergence criteria were set to 10^{-6} for all residuals of momentum, energy and continuity equation. Temperature dependent material properties of the test cell and cryostat were employed to improve solution accuracy.

The ANSYS/Fluent thermal model includes the test cell and lid, the sample stick up to the first radiation baffle, the cryostat copper block and the sample well enclosure, which is an aluminum canister secured to the copper block. These components are illustrated in Fig. 2. Heat is transferred to and from the test cell by a combination of heat conduction through the radiation baffle and sample stick as well as through convection in the helium gas surrounding the test cell and contained within the sample well enclosure. The amount of helium in the sample well surrounding the test cell could not be precisely measured and the amount of helium changes when changing out the test cell being tested. The pressure in the sample well is estimated to be between 10 Pa and 200 Pa. An added complexity arises from the helium surrounding the test cell interacting with helium in the sample well above the bottom radiation baffle, which supports a temperature gradient increasing from the bottom to the top of the cryostat. As the test cell is cooled and heated, there is net movement of helium gas between the sample well enclosure and the sample well volume above the bottom radiation baffle.

The thermal model is tuned using the transient response of the test cell and the sample well helium gas during the dry cell thermal cycling tests. The sample well enclosure, which is fabricated from aluminum 6061, is initially set to the same temperature as the copper block and the test cell. The transient temperature of the copper block is varied in the model to match the experimental results. The numerical temperatures that correspond in location to the experimental sensors, three on the test cell and one in the helium gas, are determined from the simulation and compared to the experimental values. Matching the transient response for all four sensors requires minor adjustments to the thermal diffusivity of the helium gas and contact resistance between the copper block and the bottom radiation baffle. This procedure is repeated for each test cell. Once the thermal model results match the transient sensor data, then the effective heat transfer conditions, namely contact resistances and helium gas density, for each test cell are established. These conditions are presumed to remain constant during the subsequent condensation and evaporation experiments. Fig. 4 illustrates a 'matched' transient response for one of the silicon diode sensors on the 10-mm-diameter 316L SS test cell.

After the heat transfer conditions were established for the 10-mm-diameter aluminum test cell, a grid sensitivity study for the thermal model was conducted using 20,000, 30,000, 46,000, and 65,000 nodes. After 350 s of simulation, the deviation of the numerically predicted temperature from the measured temperature at the bottom of the test cell varied between 0.9% at the two highest node counts, 1.2 percent at 30,000 nodes, and 2.15% at 20,000 nodes. A node count of 30,000 was selected as the optimum balance between accuracy and computational speed.

4. Liquid–vapor interface shape determination

Preliminary testing indicated the possibility of the existence of a contact angle of approximately 4 between liquid hydrogen and aluminum. The conical transition in the first test cell was designed to qualitatively probe the possible existence of a contact angle between hydrogen and aluminum. Fig. 3b is a neutron radiograph of liquid hydrogen in the conical section of this test cell. The notable feature is the flatness of the liquid–vapor interface despite the Bond number being approximately 9. At this Bond number, the interface will have significant curvature in a circular cylinder as seen in Fig. 5. Fig. 3c is the log transform of the normalized image. These images suggest the presence of a finite contact angle between liquid hydrogen and aluminum.

While the general consensus may be that cryogens are perfectly wetting, there are many studies that indicate wetting transitions and finite contact angles. Cheng et al. [34] investigated the wetting transition of liquid hydrogen on an alkali metal surface using a quartz microbalance. They confirmed the existence of a wetting transition temperature between 17.8 K and 18.0 K for a relative pressure of 1.0. As the relative pressure decreased (less than standard pressure), the wetting transition temperature increased. The behavior of hydrogen and helium wetting transition was used by Herminghaus et al. [35] as a model system for investigation of wetting phenomena. The wetting transition was optically investigated using a Surface Plasmon Resonance (SPR) imaging system. Droplets of liquid hydrogen were observed to form on a homogeneous film adsorbed to a gold film (used to generate the plasmons), which indicates a finite contact angle. Similarly, Ross et al. [36] observed the formation of isolated droplets of liquid hydrogen on cesium below the wetting transition temperature. They optically

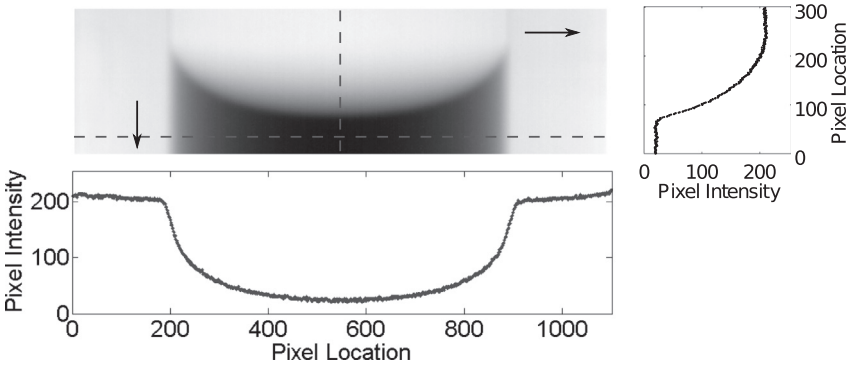

Fig. 5. Stacked and averaged images with variation in pixel intensities along the highlighted row and column.

measured the contact angle of liquid hydrogen on an alkali metal surface below the wetting transition temperature, reported as 20.6 K, and concluded that the liquid–solid interfacial energy is "not negligibly weak as has been assumed." There is also a strong possibility that viscous stresses in the contact line region due to phase change may alter the apparent contact angle of a meniscus. Krahl et al. [37], using drop tower experiments and independent computational studies, developed a dimensionless correlation of the apparent contact angle shift with a temperature difference between the substrate and the liquid phase. The correlation is based on an apparent contact angle measured at a location on the meniscus where the liquid film thickness is 140 μm. Additional experimental support for the experimentally observed and computationally predicted shift in contact angle is reported in Kulev and Dreyer [38] and Fuhrmann and Dreyer [39]. Using the correlation of Krahl et al. [37], a 4° apparent contact angle for an evaporating hydrogen meniscus requires a 0.18 K temperature difference between the liquid and the test cell wall. This temperature difference is less than the uncertainty of the experimental measurements, but within the uncertainty of the computational predictions of the thermal model.

In order to more accurately determine if a finite contact angle exists, the meniscus profiles from the cylindrical sections of the four test cells are matched to the theoretical Laplace curves. Laplace curves are determined by numerically integrating the Laplace–Young equation (Eq. (2)) for a axisymmetric cylinder in cylindrical coordinates [40].

$$\frac{df(\psi)}{d\psi} = \frac{\sin\psi}{fBo - (\sin\psi)/r + \lambda}, \quad \frac{dr(\psi)}{d\psi} = \frac{\cos\psi}{fBo - (\sin\psi)/r + \lambda}, \quad \left(0 < \psi < \frac{\pi}{2} - \theta\right) \tag{2}$$

$f(\psi) = r(\psi) = 0$ at $\psi = 0$ and $r(\psi) = 1$ at $\psi = \pi/2 - \theta$. The origin of the coordinate system lies at the center of the meniscus. $f(r)$ is the dimensionless height of the surface at a dimensionless distance r from the center, λ is twice the curvature of the meniscus at the origin and Bo is the Bond number. θ is the contact angle between the meniscus surface and the cylinder wall and $\psi = \tan^{-1}(df/dr)$ is the angle between the meniscus and a horizontal plane. The equation is solved numerically in MATLAB using `ode113` which is a variable order Adams–Bashforth–Moulton predictor–corrector solver. Once the appropriate Laplace curve is found for the hydrogen meniscus, the contact angle is the value of the first derivative of f at $r = 1$.

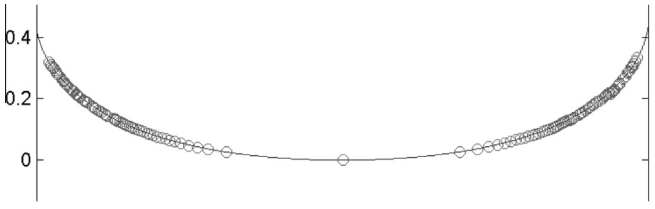

Fig. 6. Laplacian curve fit to the detected meniscus edge on stacked image of liquid hydrogen in aluminum test cell. Symbols are the meniscus edge and the line is the Laplace curve representing the best fit to the edge data.

The noise in the images posed difficulties in accurately determining the meniscus shape, especially near the test cell wall. Different types of noise are present in the images, namely salt noise (bright pixels in different locations for different images) and Poisson noise (variance in pixel intensities about a mean). Salt noise is characterized by pixels with very high intensity values, with values ranging from few times (2× to 3×) to more than 40× higher than the adjacent pixels. These are removed by replacing the hot pixels with the median intensity of the surrounding pixels intensities. Poisson noise is difficult to attenuate. At the center of the test cell the meniscus location is more accurately identified due to larger gradients in the pixel intensities at the liquid–vapor interface. Moving radially from the center, the thickness of the liquid cross-section decreases with an accompanying decrease in signal-to-noise. The total exposure time for each image is 10 s.

Poisson noise is reduced by stacking multiple images and averaging the stacked image. During evaporation or condensation, the meniscus is moving. Therefore, the image is re-centered for stacking. A sequence of stacked and averaged images is shown Fig. 5. The images have been cropped to 1101 × 301 pixels with an interior diameter of 10 mm.

The meniscus shape is determined by examining the pixel intensity variation from the liquid to the vapor along vertical columns of pixels. In the liquid the pixel intensity remains relatively constant as shown in Fig. 5. The pixel location at which the intensity drops below the average liquid intensity indicates the presence of the meniscus. The threshold for the limiting intensity is calculated by averaging the intensity of all the pixels in the vertical column constrained between the bottom of the test cell to the row corresponding to the meniscus apex. The average pixel intensity for each column of pixels varies from a minimum at the center of the test cell to a maximum at the test cell wall. Thus, the value of the limiting threshold increases automatically resulting in an adaptive threshold. The use of a fixed threshold is avoided as it alters the location of the meniscus based upon the value selected for threshold.

Once the meniscus edge is determined, the data is scaled, non-dimensionalized and fit to a Laplace curve as shown in Fig. 6. The error is calculated as the sum of the normal distance between the points on the meniscus and the Laplace curve [41]. The Laplace curve that results in the minimum error is the curve that represents meniscus. The resulting Laplace curve suggest that a contact angle of 4° ± 4° for liquid hydrogen in the 10 mm diameter aluminum test cell. The relatively large uncertainty is the result of

the image noise and the meniscus motion during imaging. The shift in meniscus position during a single 10 s exposure varied between 6 and 16 pixels depending upon the rate of evaporation or condensation. In addition, for very small contact angles the calculated contact angle is highly sensitive to the errors in the meniscus edge detection and the accuracy of meniscus edge detection to limited to ± 3 pixels.

5. Summary

A new method for imaging liquid hydrogen menisci undergoing phase change has been developed using the NIST Neutron Imaging Facility. The eventual objective is to couple the macroscale imaging to a computational thermal model and then to a microscale model of the contact line region in order to extract evaporation and condensation coefficients for liquid hydrogen. The methodology for conducting the neutron imaging experiments are discussed in detail and stable control of evaporation and condensation of hydrogen in aluminum and stainless steel cylindrical test cell was achieved. Neutron imaging experiments with liquid methane are being conducted at the time of writing this paper. The computational thermal model, necessary to predict the inner wall temperature distribution for the microscale model, accurately tracks the thermal transients of the experiment despite significant uncertainty in the mass of helium gas serving to convect heat to and from the test cell in the cryostat. Finally, initial observations suggest the existence of a non-perfectly wetting condition with hydrogen.

Disclaimer

Certain trade names and company products are mentioned in the text or identified in an illustration in order to adequately specify the experimental procedure and equipment used. In no case does such identification imply recommendation or endorsement by the National Institute of Standards and Technology, nor does it imply that the products are necessarily the best available for the purpose.

Acknowledgments

This work was supported by an Early Stage Innovations Grant from NASA's Space Technology Research Grants Program (Grant # NNX14AB05G).

References

[1] Panzarella CH, Kassemi M. On the validity of purely thermodynamic descriptions of two-phase cryogenic fluid storage. J Fluid Mech 2003;484:41–68.
[2] Panzarella C, Plachta D, Kassemi M. Pressure control of large cryogenic tanks in microgravity. Cryogenics 2004;44:475–83.
[3] Panzarella CH, Kassemi M. Self-pressurization of large spherical cryogenic tanks in space. J Spacecraft Rockets 2005;42:299–308.
[4] Barsi S, Kassemi M, Panzarella CH, Alexander JID. A tank self-pressurization experiment using a model fluid in normal gravity. AIAA2005-1143; 2005.
[5] Panzarella C, Kassemi M. One-dimensional model of evaporation and condensation in the presence of a noncondensable gas with applications to cryogenic fluid storage. Int J Heat Mass Transfer 2009;52:3767–77.
[6] Hartwig J, McQuillen J. Analysis of screen channel LAD bubble point tests in liquid oxygen at elevated temperature. In: 42nd AIAA thermophysics conference. AIAA 2011-3775, Honolulu, Hawaii; 2011.
[7] Hartwig J, McQuillen J. Analysis of screen channel LAD bubble point tests in liquid methane at elevated temperature. In: 50th AIAA aerospace sciences meeting. AIAA 2012-0759, Nashville, Tennessee; 2012.
[8] Hartwig J, McQuillen J, Chato D. Performance gains of propellant management devices for liquid hydrogen depots. In: 51st AIAA aerospace sciences meeting. AIAA 2013-0368, Grapevine, Texas; 2013.
[9] Plawsky JL, Ojha M, Chatterjee A, Wayner Jr PC. Review of the effects of surface topography, surface chemistry and fluid physics on evaporation at the contact line. Chem Eng Commun 2008;196:658.
[10] Preiss G, Wayner Jr PC. Evaporation from a capillary tube. J Heat Transfer 1976;98:178–81.
[11] Ajaev VS. Interfacial fluid mechanics. US, Boston, MA: Springer; 2012.
[12] Wayner Jr PC. The effect of interfacial mass transport on flow in thin liquid films. Colloids Surf 1991;52:71.
[13] Panchamgam S, Chatterjee A, Plawsky J, Wayner P. Comprehensive experimental and theoretical study of fluid flow and heat transfer in a microscopic evaporating meniscus in a miniature heat exchanger. Int J Heat Mass Transfer 2008;51:5368–79.
[14] Potash J, Wayner MJ, Peter C. Evaporation from a two-dimensional extended meniscus. Int J Heat Mass Transfer 1972;15:1851–63.
[15] Derjaguin B, Nerpin S, Churayev N. Effect of film transfer upon evaporation of liquids from capillaries. Bull Rilem 1965;29:93–8.
[16] DasGupta S, Kim IY, Wayner JPC. Use of the Kelvin–Clapeyron equation to model an evaporating curved microfilm. J Heat Transfer 1994;116:1007–15.
[17] Holm FW, Goplen SP. Heat transfer in the meniscus thin film transition region. J Heat Transfer 1979;101:543.
[18] Moosman S, Homsy GM. Evaporating menisci of wetting fluids. J Colloid Interface Sci 1980;73:212–23.
[19] Swanson LW, Herdt GC. Model of the evaporating meniscus in a capillary tube. J Heat Transfer 1992;114:434–41.
[20] Schmidt GR. Thermocapillary flow with evaporation and condensation and its effect on liquid retention in low-G fluid acquisition devices. NASA TP-3463; 1994.
[21] Pratt DM, Hallinan KP. Thermocapillary effects on the wetting characteristics of a heated curved meniscus. J Thermophys Heat Transfer 1997;11:519.
[22] Schonberg JA, DasGupta S, Wayner Jr PC. An augmented Young–Laplace model of an evaporating meniscus in a microchannel with high heat flux. Exp Therm Fluid Sci 1995;10:163.
[23] Ha V-M, Lai C-L. Theoretical analysis of Marangoni instability of an evaporating droplet by energy method. Int J Heat Mass Transfer 2004;47:3811.
[24] Panchamgam SS, Gokhale SJ, Plawsky JL, DasGupta S, Peter J, Wayner C. Experimental determination of the effect of disjoining pressure on shear in the contact line region of a moving evaporating thin film. J Heat Transfer 2005;127:231.
[25] Du S-Y, Zhao Y-H. New boundary conditions for the evaporating thin-film model in a rectangular micro channel. Int J Heat Mass Transfer 2011;54:3694–701.
[26] Wee S-K, Kihm KD, Hallinan KP. Effects of the liquid polarity and the wall slip on the heat and mass transport characteristics of the micro-scale evaporating transition film. Int J Heat Mass Transfer 2005;48:265–78.
[27] Wee S-K, Kihm KD, Pratt DM, Allen JS. Microscale heat and mass transport of evaporating thin film of binary mixture. J Thermophys Heat Transfer 2006;20:320.
[28] Fritz III DL. An implementation of a phenomenological evaporation model into a porous network simulation for water management in low temperature fuel cells. PhD thesis. Michigan Technological University; 2012.
[29] Schrage RW. A theoretical study of interphase mass transfer. New York: Columbia University Press; 1953.
[30] Cammenga HK, Klinge H, Rudolph BE. Untersuchungen über die Verdampfungsgeschwindigkeit von Flüssigkeiten. Fortschrittsberichte über Kolloide und Polymere 1971;55:118.
[31] Marek R, Straub J. Analysis of the evaporation coefficient and the condensation coefficient of water. Int J Heat Mass Transfer 2001;44:39–53.
[32] Hussey D, Jacobson D, Arif M, Huffman P, Williams R, Cook J. New neutron imaging facility at the NIST. In: Proceedings of the fifth international topical meeting on neutron radiography ITMNR-5 fifth international topical meeting on neutron radiography. Nucl Instrum Methods Physics Res Sect A: Accelerat, Spectrom, Detect Assoc Equip, 542. p. 9–15.
[33] Hussey DS, Jacobson DL, Arif MM, Coakley KJ, Vecchia D. In situ fuel cell water metrology at the NIST neutron imaging facility. ASME J Fuel Cell Sci Technol 2010;7:021024-1–4-6.
[34] Cheng E, Mistura G, Lee HC, Chan MHW, Cole MW, Carraro C, et al. Wetting transitions of liquid hydrogen films. Phys Rev Lett 1993.
[35] Herminghaus S, Vorberg J, Gau H, Conradt R, Reinelt D, Ulmer H, et al. Hydrogen and helium films as model systems of wetting. Ann Physik 1997.
[36] Ross D, Taborek P, Rutledge JE. Wetting behavior of h_2 on cesium. Phys Rev B: Condens Matter Mater Phys 1998;58:R4274–6.
[37] Krahl R, Gerstmann J, Behruzi P, Bansch E, Dreyer ME. Dependency of the apparent contact angle on nonisothermal conditions. Phys Fluids 2008.
[38] Kulev N, Dreyer M. Drop tower experiments on non-isothermal reorientation of cryogenic liquids. Microgravity Sci Technol 2010;22:463–74.
[39] Fuhrmann E, Dreyer ME. Heat and mass transfer at a free surface with diabatic boundaries in a single-species system under microgravity conditions. Exp Fluids 2014;55:1–18.
[40] Concus P. Static menisci in a vertical right circular cylinder. J Fluid Mech 1968;34:481–95.
[41] Hoorfar M, Neumann AW. Recent progress in axisymmetric drop shape analysis (ADSA). Adv Colloid Interface Sci 2006;121:25–49.